

# Combining the Masking and Scaffolding Modalities of Colloidal Crystal Templates: Plasmonic Nanoparticle Arrays with Multiple Periodicities

Shikuan Yang,<sup>\*,†</sup> Daniel Slotcavage,<sup>†</sup> John D. Mai,<sup>‡</sup> Wansheng Liang,<sup>§</sup> Yuliang Xie,<sup>†</sup> Yuchao Chen,<sup>†</sup> and Tony Jun Huang<sup>\*,†</sup>

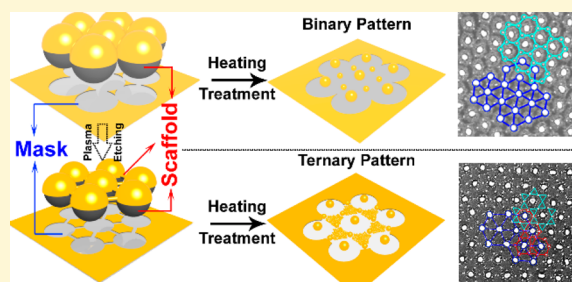
<sup>†</sup>Department of Engineering Science and Mechanics, The Pennsylvania State University, University Park, State College, Pennsylvania 16802-6812, United States

<sup>‡</sup>Department of Mechanical and Biomedical Engineering, City University of Hong Kong, Kowloon, Hong Kong SAR

<sup>§</sup>Department of Nuclear Medicine, Lanzhou General Hospital of Lanzhou Military Area Command, Lanzhou 730050, China

## S Supporting Information

**ABSTRACT:** Surface patterns with prescribed structures and properties are highly desirable for a variety of applications. Increasing the heterogeneity of surface patterns is frequently required. This work opens a new avenue toward creating nanoparticle arrays with multiple periodicities by combining two generally separately applied modalities (i.e., scaffolding and masking) of a monolayer colloidal crystal (MCC) template. Highly ordered, loosely packed binary and ternary surface patterns are realized by a single-step thermal treatment of a gold thin-film-coated MCC and a nonclose-packed MCC template. Our approach enables control of the parameters defining these nanoscale binary and ternary surface patterns, such as particle size, shape, and composition, as well as the interparticle spacing. This technique enables preparation of well-defined binary and ternary surface patterns to achieve customized plasmonic properties. Moreover, with their easy programmability and excellent scalability, the binary and ternary surface patterns presented here could have valuable applications in nanophotonics and biomedicine. Specific examples include biosensing via surface-enhanced Raman scattering, fabrication of plasmonic-enhanced solar cells, and water splitting.



## 1. INTRODUCTION

Nanopatterns on a substrate surface play diverse roles in a wide range of application areas, from semiconductors,<sup>1–3</sup> plasmonics,<sup>4–9</sup> photonics,<sup>10–12</sup> and sensors,<sup>13–15</sup> to field emitters<sup>16</sup> and biomedicine.<sup>17–21</sup> Often, multiple properties desired for specific applications can be obtained by increasing the heterogeneity of the nanostructure arrays.<sup>22</sup> Composed of either one type of nanostructure arranged in different geometries or several types of nanostructures (e.g., with different sizes, shapes, compositions, or orientations) arranged in the same or different geometric patterns,<sup>23–25</sup> nanostructure arrays with multiple periodicities are particularly attractive due to their programmability and flexibility in producing desired chemical and structural features.<sup>5</sup> There are already a variety of lithographic methods used to create surface patterns of nanostructures including electron beam lithography,<sup>26</sup> optical lithography,<sup>27</sup> and focused ion beam etching.<sup>28</sup> However, these lithographical methods are usually expensive, time-consuming, and inefficient for creating complex surface patterns. In contrast, colloidal lithography has been developed rapidly as a low-cost, high throughput, and efficient technique for fabrication of two-dimensional surface patterns.<sup>29–39</sup> For example, by using a monolayer colloidal crystal (MCC)

template, composed of closely packed polystyrene (PS) spheres, as a mask during thermal or sputtering deposition of a thin film, honeycomb arrays of nanotriangles, nanorings, nanorods, and nanocrescents can be easily prepared after removing the PS spheres.<sup>29–34</sup> Comparatively, hexagonally arranged hollow sphere or micropillar arrays can be created by growing materials on the MCC template behaving as a scaffold employing the electrochemical deposition or pulsed laser deposition methodologies.<sup>35–39</sup> Building units in these surface patterns created by the colloidal lithography approach are limited to be either hexagonally arranged or in a honeycomb pattern. Therefore, new concepts that can increase the heterogeneity of surface patterns created by colloidal lithography methods are crucial in expanding the application fields of conventional colloidal lithography technique.

In this work, by merging the masking and scaffolding modalities of the MCC template, we developed a unique single-step process for creating binary and ternary patterns on a surface over large areas (>1 cm<sup>2</sup>) with excellent structural

Received: August 4, 2014

Revised: October 21, 2014

Published: October 22, 2014

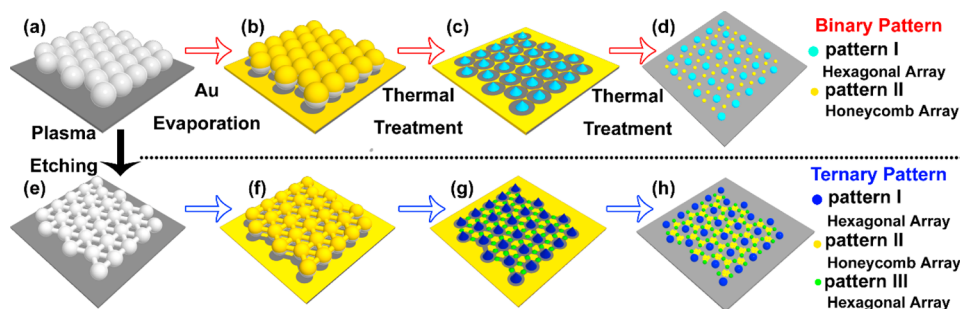


**Figure 1.** Schematic illustration of the binary and ternary surface patterns fabricated by merging the masking and scaffolding modalities of the MCC template. (a) MCC template. (b) After Au film evaporation. (c) After thermal treatment at low temperatures ( $<350\text{ }^{\circ}\text{C}$ ). (d) After thermal treatment at high temperatures ( $>400\text{ }^{\circ}\text{C}$ ). (e) Nonclose-packed MCC template obtained by plasma etching of the MCC template. (f) After Au film evaporation. (g) After thermal treatment at low temperatures ( $<350\text{ }^{\circ}\text{C}$ ). (h) After thermal treatment at high temperatures ( $>400\text{ }^{\circ}\text{C}$ ). To distinguish different pattern structures, yellow, cyan, blue, and green colors are all Au nanoparticles.

programmability. Each unit of the binary surface pattern consists of a large central particle and six satellite particles, realized by a controllable deformation of the gold-coated MCC template and a thermodynamically driven dewetting process. Ternary surface patterns composed of nanoparticles with two different sizes arranged in different geometries, as well as hexagonally arranged nanoparticle clusters, can be obtained using a nonclose-packed gold-coated MCC template. The structure of the binary and ternary patterns can be conveniently predesigned and adjusted by varying parameters that influence the template deformation and/or the dewetting processes. Surface patterns with such complicated structures are almost inaccessible using traditional fabrication concepts. By tailoring the structure of the Au nanoparticle patterns or simply tilting the incident angle of the excitation illumination, the localized surface plasmon resonance (LSPR) peaks can be maneuvered over a broad range of wavelengths in a highly controllable manner. With their tunable plasmonic properties and excellent programmability, we believe these loosely packed binary and ternary Au surface patterns can be valuable in applications such as LSPR-based and surface-enhanced Raman scattering (SERS)<sup>2</sup> sensing, plasmonic-enhanced solar cells,<sup>40,41</sup> and water splitting.<sup>42</sup>

## 2. RESULTS AND DISCUSSION

**2.1. Surface Patterning Mechanism.** By combining the masking with the scaffolding modalities of the MCC template, we developed a unique single-step process for creating binary and ternary patterns on a surface over large areas ( $>1\text{ cm}^2$ ). The fabrication concept is shown in Figure 1. A large area, uniformly structured MCC template composed of PS spheres was prepared by a spin-coating process (Figure 1a).<sup>14,29–39</sup> After fixing the MCC template on the underneath Si substrate by heating at  $110\text{ }^{\circ}\text{C}$  for 5 min, a thin layer of Au film was thermally evaporated on the MCC template (Figure 1b). Due to the shadow effects, only the top surface of the PS spheres was coated by the Au film.<sup>37</sup> Also, Au film was deposited through the interstices between three adjacent PS spheres, forming a honeycomb array constituted by Au nanotriangles. Subsequent thermal treatments of the Au-coated MCC template at elevated temperatures ( $<350\text{ }^{\circ}\text{C}$ ) led to decomposition of the PS spheres. Strikingly, the position of the PS spheres was kept almost unchanged during the thermal deformation and decomposition process. Eventually, Au film evaporated on the PS spheres was loaded onto the substrate, which accurately occupied the original position of the PS

spheres (Figure 1c). Dewetting process of the Au film took place at high heating temperatures ( $>400\text{ }^{\circ}\text{C}$ ), resulting in the transformation of the Au film originally deposited on the PS spheres into Au nanoparticles. These Au nanoparticles are hexagonally arranged, forming pattern I. During the creation of pattern I, the MCC template was used as a scaffold. The Au nanotriangles evaporated on the Si substrate using the MCC template as a mask also suffered from dewetting processes, evolving into a honeycomb array composed of spherical Au nanoparticles (pattern II). The nanoparticles defining pattern II fit comfortably into the lattice gaps of pattern I, resulting in a binary surface pattern (Figure 1d). Plasma etching can transform the MCC templates into nonclose-packed ones (Figure 1e). Interestingly, bridges were formed between two adjacent PS spheres. After heating the Au-coated nonclose-packed MCC template (Figure 1f), Au film evaporated on the PS spheres evolved into pattern I composed of hexagonally arranged Au nanoparticles. While Au quasi-triangles deposited on the substrate developed into nanoparticle clusters (pattern II). Meanwhile, Au film evaporated on the bridges finally evolved into pattern III. Patterns I, II and III weaved together, giving rise to a ternary surface pattern (Figure 1g,h). In short, complex surface patterns can be fabricated by employing the MCC template as a mask and a scaffold simultaneously.

**2.2. Preparation of MCC and Nonclose-Packed MCC Template.** Figure 2a shows a typical MCC template composed of closely packed PS spheres with  $1\text{ }\mu\text{m}$  size over a large area (Figure 2a, inset). Only the top surface of the PS spheres was covered by the Au layer during Au thermal evaporation process (Figure 2b), as the bottom halves of the spheres were shielded by shadow effects. Nonclose-packed MCC template can be prepared by plasma etching of the as-prepared MCC template. After the MCC template was plasma treated for 30 min, a nonclose-packed MCC template composed of PS spheres with approximately  $900\text{ nm}$  size was synthesized (Figure 2c). Interestingly, there was a bridge between two neighboring PS spheres (Figure 2d).

**2.3. Surface Pattern Characterization.** After heating the Au film-covered MCC template at  $450\text{ }^{\circ}\text{C}$  for 3 h, a well-ordered surface pattern composed of Au particles with a mean diameter of  $320\text{ nm}$  was created, evolved from the Au film evaporated on the PS spheres (Figure 3a, pattern I). Within the surface pattern, each Au nanoparticle has six closest neighbors. This differs from patterns produced by the conventional colloidal lithography method, in which each nanoparticle has only three closest neighbors (Supporting Information, Figure

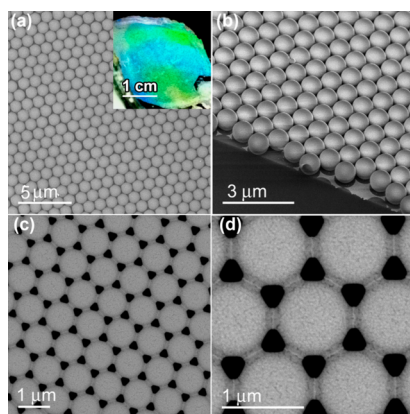


**Figure 2.** (a) Large area and uniformly structured MCC template composed of closely packed 1  $\mu\text{m}$  PS spheres; (inset) photograph of the MCC template. (b) Au film evaporated on the top surface of the MCC template. (c) Nonclose-packed MCC template created by plasma etching of the MCC template. (d) Bridges formed between adjacent PS spheres.

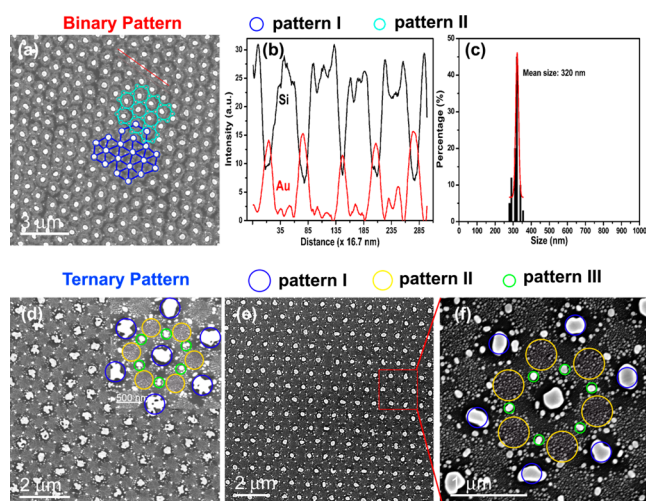


**Figure 3.** (a) A binary surface pattern obtained by heating a 10 nm gold-coated MCC template at 450  $^{\circ}\text{C}$  for 3 h. (b) SEM line-scan result across the red line drawn in panel a. (c) Size distribution of the Au particles in pattern I. (d) Ternary surface pattern created by heating the Au thin-film-covered, nonclose-packed MCC template at 350  $^{\circ}\text{C}$  for 3 h; (inset) structure of patterns I, II, and III. (e and f) Ternary surface pattern fabricated by the thermal treatment at 450  $^{\circ}\text{C}$  for 3 h.

S1). The scanning electron microscope (SEM) line-scan result (across the line drawn in Figure 3a) clearly demonstrated the composition of the nanoparticles and the regularity of pattern I (Figure 3b). Because the Au nanoparticles were transformed from the Au films evaporated on the PS spheres with the same thickness and thus volume, the size distribution of the Au nanoparticles is very narrow (Figure 3c). Meanwhile, the Au nanotriangles thermally deposited on the substrate evolved into spherical Au nanoparticles, forming pattern II (Figure 3a). In pattern II, each Au nanoparticle has three closest neighbors (Figure 3a). Pattern II embedded itself into the lattices of pattern I, giving rise to a complex “solar system” pattern. Each “solar system” consists of one large nanoparticle surrounded by six other large nanoparticles and six small nanoparticles. Similarly, each small nanoparticle is surrounded by three other small nanoparticles and three large nanoparticles (Figure 3a). These Au nanoparticles strongly attach onto the Si

substrate, facilitating diverse on-substrate applications. The complexity of this binary surface pattern enables tunable plasmonic properties,<sup>46</sup> which will be discussed later.

As mentioned above, increasing the heterogeneity of surface nanopatterns is frequently required but extremely challenging using conventional colloidal lithography technique. Therefore, we further explored how to prepare nanopatterns on a surface with more complex structures by using the concept developed here, that is, merging the masking and scaffolding modalities of the MCC templates. The preheating treatment of the MCC template at 110  $^{\circ}\text{C}$  for 5 min can connect the neighboring PS spheres tightly. During the subsequent plasma etching treatment, the etching rate at the connection area is much slower than at other areas, resulting in the formation of bridges between neighboring PS spheres after the MCC template was plasma treated for 30 min (Figure 2d). We expect that these bridges can also behave as scaffolds during subsequent thermal treatments of the Au-covered plasma-treated MCC template. As anticipated, the Au film evaporated on these bridges finally evolved into small Au nanoparticles (about 80 nm) arranged in a hexagonal geometry (pattern III) after calcination (Figure 3d–f). Similar to the case of heating the Au film-covered MCC template, pattern I was composed of hexagonally arranged large Au nanoparticles (about 240 nm in diameter), evolved from Au film evaporated on those PS spheres in the nonclose-packed MCC template. Clusters composed of many about 20 nm Au nanoparticles were arranged in a honeycomb geometry deposited on the substrate through the interstices between adjacent PS spheres. As a result, a uniform ternary nanopattern was prepared over a large surface area using the plasma-exposed MCC template (Figure 3d,e). By adjusting the plasma-etching time of the MCC template, the diameter of the PS spheres and the subsequent length of the bridges can be controlled, which can be further used to control the structure of the ternary patterns. Surprisingly, those 20 nm Au nanoparticles in pattern II did not fuse into large ones, even after a heating treatment at 650  $^{\circ}\text{C}$  for 3 h. The abnormal stability of these Au nanoparticles is still under investigation. One of the possible reasons is the original Au triangles deposited on the substrate using the nonclose-packed MCC template is very uniform in thickness. The uniform thickness of the large Au triangles enables simultaneous nucleation of holes within the Au triangles during thermal-induced dewetting processes.<sup>43–45</sup> Subsequently, the Au triangles break down into numerous small Au nanoparticles with almost the same size. These Au nanoparticles with a similar size have a low chance to grow by consuming adjacent particles even at high heating temperatures.<sup>43–45</sup> Owing to the high density of the Au nanoparticles in pattern II, a significant amount of SERS “hot spots” existed within the ternary surface patterns. Thus, the ternary surface nanopatterns are good candidates for SERS substrates. Using 4-aminothiophenol as a test molecule, we estimated the enhancement factor of the ternary surface patterns to be  $>10^7$  (Supporting Information, Figure S2).

**2.4. Control of Multiple Structures within a Binary Pattern.** Precise manipulation of the final structure of the binary pattern on the surface can be achieved by using different sized PS spheres and tuning the Au layer thickness. For instance, adopting an MCC template comprised of large PS spheres can increase the Au nanoparticle size and the interparticle spacing in the final pattern at the same time. Some applications, however, demand independent control of nanoparticle size and interparticle spacing.<sup>46</sup> Varying the



thickness of the Au layer offers a convenient solution to change the nanoparticle size while keeping the interparticle distance constant. To demonstrate independent control of nanoparticle size, a binary pattern composed of 230 and 75 nm Au nanoparticles (Supporting Information, Figure S3), was fabricated using MCC templates composed of 1  $\mu\text{m}$  PS spheres by increasing the thickness of the evaporated Au film from 10 to 20 nm. The unique patterning technique described here offers another major advantage over other surface patterning methods: the final nanoparticle size and spacing can be precalculated without the need for experimentation.

The size of the Au particles in pattern I is directly determined by the volume of the Au layer evaporated on the PS spheres. This is related to both the diameter of the PS spheres and the thickness of the evaporated Au film. Assuming that the final resulting Au particles are perfectly spherical, the radius ( $r_1$ ) of the Au particles can be calculated based on eq 1:

$$\frac{4}{3}\pi r_1^3 = \pi R^2 h \quad (1)$$

where  $R$  is the radius of the PS spheres;  $h$  is the thickness of the Au film; and  $r_1$  is the radius of the Au particles in pattern I. In pattern II, the volume of the Au nanotriangles determines the final radius ( $r_2$ ) of the Au nanoparticles, as described by eq 2:

$$\frac{4}{3}\pi r_2^3 = \left(\sqrt{3}R^2 - \frac{\pi}{2}R^2\right)h \quad (2)$$

If we designate the large and small particles as A and B, respectively, then the stoichiometry of the loosely packed binary surface pattern is exactly  $\text{AB}_2$ . Comparing eqs 1 and 2 shows that the expected radius ratio  $r_1/r_2$  in the loosely packed binary pattern should be about 2.7. By slightly heating the MCC template before Au film evaporation, the void between three adjacent PS spheres can be controllably shrunk.<sup>47</sup> As a result, the ratio  $r_1/r_2$  can be further increased. Using the experimental parameters ( $R = 500$  nm,  $h = 10$  nm), eqs 1 and 2 predict values of 125 and 45 nm for  $r_1$  and  $r_2$ , respectively. Experimental results yielded slightly larger nanoparticle diameters (160 and 55 nm for  $r_1$  and  $r_2$ , respectively) than predicted. The difference in the calculated and experimental results is attributed to imperfections in the spherical shape of the synthesized gold nanoparticles. On the basis of these calculations, we predicted an approximately  $90^\circ$  contact angle between the Au nanoparticle and the Si substrate. After considering the almost hemispherical shape of the Au nanoparticles, accurate prediction of  $r_1$  and  $r_2$  can be achieved.

Importantly, the surface patterning technique developed here can be immediately extended to the preparation of binary and ternary surface patterns composed of other materials (e.g., silver, platinum, copper, and even alloys). In a negative control experiment, we heated a layer of Au film without the MCC templates. As expected, an irregular array of nanoparticles with a wide range of size distributions were created on the surface by a heterogeneous dewetting process (Supporting Information, Figure S4).<sup>43–45</sup>

**2.5. Surface Pattern Formation Process.** To understand the formation process of the binary patterns, morphologies of the Au-coated MCC template at different heating temperatures were monitored. As can be seen in Figure 4, the mean size of the PS spheres was reduced from 1  $\mu\text{m}$  to 625 nm (Figure 4a,b), from 1  $\mu\text{m}$  to 565 nm (Figure 4c,d), and from 1  $\mu\text{m}$  to 480 nm (Figure 4e,f) after 3 h of heating at 200, 250, and 300  $^\circ\text{C}$ , respectively. The size decrease is caused by thermal

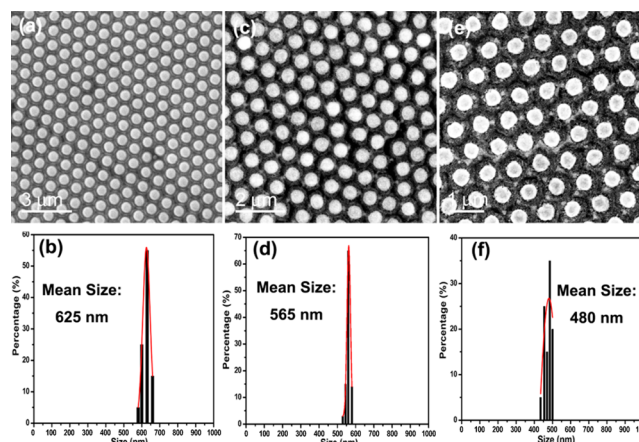


**Figure 4.** Structural evolutions of the 10 nm gold layer-coated MCC templates after thermal annealing at different temperatures for 3 h: (a) 200, (c) 250, and (e) 300  $^\circ\text{C}$ . (b, d, and f) Corresponding size distributions.

decomposition of PS spheres. The Au film adjusted its morphology accordingly by adapting to conform to the now smaller PS spheres. Under lower temperature thermal treatment ( $<450$   $^\circ\text{C}$ ), the PS spheres changed their locations slightly due to the slow deformation and decomposition rate. Thermal treatment at temperatures greater than 450  $^\circ\text{C}$  induced dewetting in the Au film, as the Au nanostructures have significantly lower melting temperatures than bulk Au.<sup>48</sup> Dewetting of the Au film resulted in the formation of solid Au nanoparticles, and gave rise to the binary and ternary patterns on the surface (Figure 3). To avoid the movement of PS spheres during the template deformation process, the Au-covered MCC template should be placed exactly horizontally in the furnace during calcination to prepare the binary and ternary patterns. It might be able to shift the position of pattern I relative to pattern II by tilting the Au-covered MCC template during thermal treatments, arising from the gravity induced homogeneous movement of the molten PS spheres.

**2.6. Plasmonic Properties of the Binary Surface Patterns.** We further studied the plasmonic properties of the prepared binary surface patterns. Varying the structure of the Au binary pattern produced measurable changes in the LSPR peaks. The original 10 nm thick Au-film-coated MCC template formed by 1  $\mu\text{m}$  PS spheres generated four LSPR peaks (Figure 5a, curve a). After the template was heated at 200  $^\circ\text{C}$  for 3 h, one of the original LSPR peaks disappeared, while the other three showed distinct shifts (curve b in Figure 5a). Heating the template at 250  $^\circ\text{C}$  or above eliminated yet another peak, leaving two prominent peaks around 560 (curves c–f, Figure 5a, referred to as peak I) and 1200 nm (referred to as peak II). These two peaks, located in the visible and near-infrared range, blue-shifted dramatically with increases in heating temperature (Figure 5b), offering a robust technique to control the plasmonic properties of the binary patterned surface.

The above results clearly demonstrate that the plasmonic properties of the binary surface patterns are sensitive to the structure (e.g., size and shape) of the Au nanoparticles. To further study the LSPR dependence on the surface layout, we investigated the plasmonic properties of the binary surface patterns prepared using MCC templates composed of different sized PS spheres (Supporting Information, Figure S5). When the templates were heated for 3 h at 200  $^\circ\text{C}$ , the binary patterns

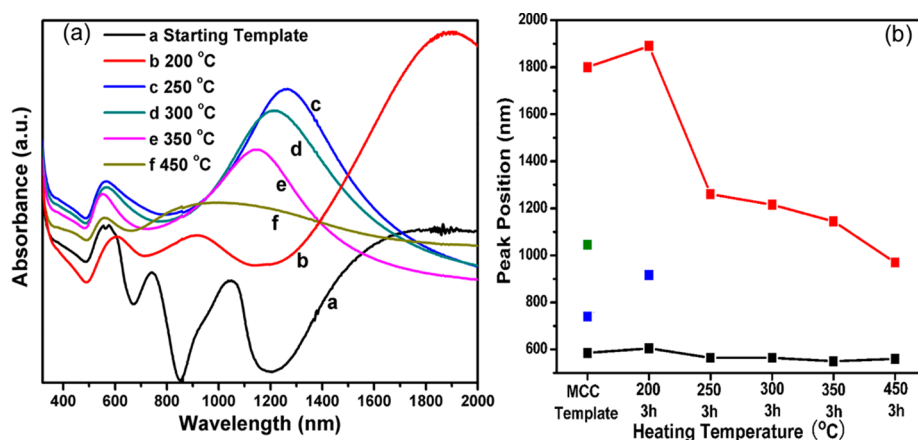


**Figure 5.** (a) Plasmonic properties of the binary surface patterns with different structures prepared at different heating temperatures. (b) LSPR peak changes resulting from different preparation conditions. The black and red curves show changes in the position of peak I and peak II, respectively, at different heating conditions.

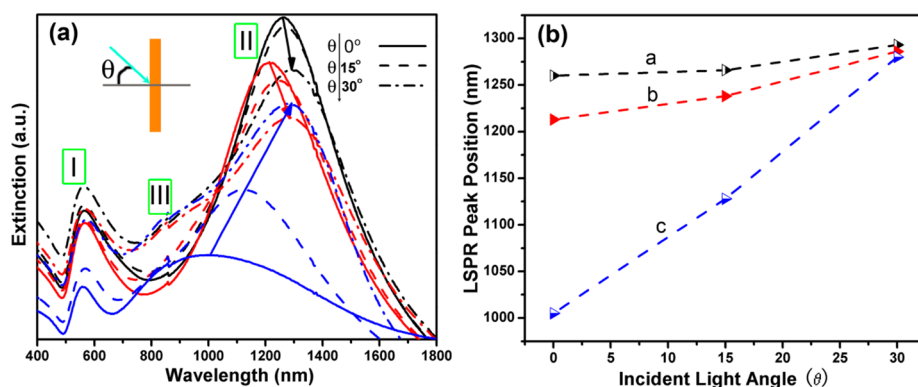


**Figure 6.** (a) Plasmonic properties of the binary nanopatterned surfaces. Black, red, and blue curves are the extinction spectra of surface patterns generated at 300, 350, and 450 °C, respectively, for 3 h. Solid, dashed, and dash-dot curves correspond to the extinction spectra at incident angles of 0°, 15°, and 30°, respectively. (Inset) Diagram defining the incident angle of the light. (b) The LSPR peak II shifts as the incident angle of the light varies.

derived from 500 nm PS spheres presented two LSPR peaks located at approximately 600 and 1100 nm. A higher heating temperature (i.e., 350 °C) led to an obvious blue shift of the two LSPR peaks. Binary patterns created using MCC templates with 200 nm PS spheres exhibited much different plasmonic properties. After heating at 200 °C for 3 h, LSPR peaks emerged at 700 and 1400 nm. More discrepancies emerged after heating at 350 °C for 3 h. A new weak peak appeared at approximately 600 nm, and the smaller peak at 1400 nm disappeared. The plasmonic properties we observed were all highly dependent on the surface layout (e.g., interparticle spacing) of the binary surface patterns.

The structure-dependence of the plasmonic properties can be explained theoretically. On the basis of previous theoretical and experimental studies,<sup>49–51</sup> because the resonance frequency of the 110 nm Au hemispheres is perfectly matched with the position of peak I, we believe that peak I in Figure 5 originates directly from the satellite Au nanoparticles in pattern II in the binary surface patterns. Adjusting the heating temperatures resulted in changes in particle size and shape, and thus induced movement of the plasmon resonance peaks. We observed that particle shrinking induced by the thermal treatment gave rise to a slight blue shift in peak I (Figure 5), in agreement with the results predicted by Mie theory.<sup>49</sup>

Peak II, however, occurs due to the plasmon coupling of adjacent Au nanoparticles within the binary surface patterns. Plasmon coupling theories suggest that a reduction in plasmon coupling, caused by an increase in the interparticle distance, should result in a blue shift in the LSPR peaks.<sup>49–51</sup> In our case, as the heating temperature increases, the nanoparticle size decreases due to dewetting-induced shrinkage. Simultaneously, the interparticle distance increases, causing weakened plasmonic coupling and, in turn, a blue shift in peak II. Finite-difference time-domain (FDTD) simulation results (Supporting Information, Figure S6) qualitatively agree with the experimental observation. Peak III in the FDTD-simulated spectrum appears when we tilt the excitation light, as discussed below.

Because binary surface patterns have a higher spatial density of nanoparticles than conventional surface patterns, plasmonic coupling gives rise to a strong LSPR peak located in the near-infrared range (~1200 nm). This peak, along with the other LSPR peak located in the visible range, make binary surface patterns promising in applications such as solar cells (to enable solar energy collection from the visible to the near-infrared range) and biomedicine.<sup>40–42,52,53</sup> It is worth mentioning that at low heating temperatures, the PS spheres were not totally removed. In this case, the ordered structure of the MCC templates in conjunction with the hollow Au hemispheres

demonstrated a strong absorbance in a specific range of wavelengths. The features of the UV–vis spectrum in those wavelengths were complex (demonstrating hybridized plasmonic-photonic characteristics),<sup>54</sup> and lie outside the scope of this study. Similar phenomena can also be used to explain the plasmonic changes in the binary patterns derived from MCC templates formed from 200 and 500 nm PS spheres.

**2.7. Angle-Dependent Plasmonic Properties.** Next, we explored the angle-dependent plasmonic properties of the binary surface patterns (Figure 6a). As the excitation angle increases, peak I exhibits no discernible movement regardless of the structure of the binary patterns, which further supports our hypothesis on the origin of peak I. Peak II, however, dramatically changes with the excitation angle (Figure 6b). This means that simply adjusting the excitation angle offers a robust method to easily and precisely maneuver the two LSPR peaks separately. A new peak (i.e., peak III) appeared at large tilt angles of the excitation light. Specifically, a new LSPR peak appeared at about 800 nm as the excitation angle reaches 30° (Figure 6). Further increasing  $\theta$  (e.g., 45°) renders a continuous red shift of peak II (Supporting Information, Figure S7). This occurs because the distance between the core and the satellite Au nanoparticles varies as  $\theta$  changes, which subsequently influences the plasmonic coupling effect.<sup>55</sup> Shrinkage of some lattices within the binary surface patterns leads to the dramatic red shift of the LSPR peaks. Those distorted lattices at large excitation angles induce the emergence of peak III. A schematic image (Supporting Information, Figure S8) and detailed discussions of the angle-dependence of the plasmonic properties can be found in the Supporting Information. In short, by simply tuning the excitation angle, the position and intensity of the two LSPR peaks can be individually manipulated over a broad range.

### 3. CONCLUSION

In summary, we have demonstrated a scalable and robust method to prepare highly ordered, loosely packed binary and ternary patterns on surfaces by combining the two modalities (i.e., scaffolding and masking) of the MCC templates. The structure of the binary or ternary patterns can be conveniently controlled and programmed. The size, shape, and composition of the nanoparticles in the binary and ternary patterns, as well as the interparticle distance, can be manipulated by tuning the thickness of the evaporated metal film, varying the heating parameters, changing the deposited materials, and employing PS spheres of different diameters in the MCC template. In addition, precalculation of nanoparticle size can be achieved, enabling precise design of surface patterns with desired plasmonic properties. Plasmonic properties are highly dependent upon the size and spacing of the core and satellite Au nanoparticles in the complex patterns. Therefore, the plasmonic properties are highly tunable through pattern structure manipulation. Furthermore, by tilting the excitation angle, LSPR peak positions can be individually shifted over a broad range, further enhancing the programmability of the patterns' plasmonic properties. With their advantages in large-scale fabrication, highly ordered and programmable structures, and highly tunable plasmonic properties, the binary and ternary surface patterns presented here can be valuable in applications such as nanophotonics, SERS sensors, solar cells, water splitting, and biomedicine.

## ■ ASSOCIATED CONTENT

### Supporting Information

Experimental details, SEM images of a honeycomb array prepared using conventional colloidal lithography method, SERS spectrum of the ternary surface nanopatterns, additional SEM images of the binary surface nanopatterns, FDTD simulations, and angle-dependent plasmonic properties of the binary surface nanopatterns prepared at different heating temperatures. This material is available free of charge via the Internet at <http://pubs.acs.org>.

## ■ AUTHOR INFORMATION

### Corresponding Authors

\*E-mail: [szy2@psu.edu](mailto:szy2@psu.edu).

\*E-mail: [junhuang@psu.edu](mailto:junhuang@psu.edu).

### Author Contributions

The manuscript was written through contributions of all authors. All authors have given approval to the final version of the manuscript.

### Notes

The authors declare no competing financial interest.

## ■ ACKNOWLEDGMENTS

We acknowledge R. C. Kogen, B. D. Kryzer, F. Guo, P.-H. Huang, and Y. H. Zhao of the Pennsylvania State University for editing the manuscript. We gratefully acknowledge the financial support from the National Institutes of Health (Director's New Innovator Award, 1DP2OD007209-01), the National Science Foundation, and the Penn State Center for Nanoscale Science (MRSEC) under grant DMR-0820404. Components of this work were conducted at the Penn State node of the NSF-funded National Nanotechnology Infrastructure Network.

## ■ REFERENCES

- (1) Paquet, C.; Kumacheva, E. *Adv. Funct. Mater.* **2007**, *17*, 3105.
- (2) Lei, Y.; Yang, S. K.; Wu, M. H.; Wilde, G. *Chem. Soc. Rev.* **2011**, *40*, 1247.
- (3) Ye, X. Z.; Qi, L. M. *Nano Today* **2011**, *6*, 608.
- (4) Yang, S. K.; Xu, F.; Ostendorp, S.; Wilde, G.; Zhao, H.; Lei, Y. *Adv. Funct. Mater.* **2011**, *21*, 2446.
- (5) Hong, S.; Kang, T.; Choi, D.; Choi, Y.; Lee, L. P. *ACS Nano* **2012**, *6*, 5803.
- (6) Liu, Z.; Wei, Q.; Zhang, X. *Nano Lett.* **2005**, *5*, 957.
- (7) Ctistis, G.; Papaioannou, E.; Patoka, P.; Gutek, J.; Fumagalli, P.; Giersig, M. *Nano Lett.* **2009**, *9*, 1.
- (8) Retsch, M.; Tamm, M.; Bocchio, N.; Horn, N.; Forch, R.; Jonas, U.; Kreiter, M. *Small* **2009**, *5*, 2105.
- (9) Unger, A.; Rietzler, U.; Berger, R.; Kreiter, M. *Nano Lett.* **2009**, *9*, 2311.
- (10) Vogel, N.; de Viguier, L.; Jonas, U.; Weiss, C. K.; Landfester, K. *Adv. Funct. Mater.* **2011**, *21*, 3064.
- (11) Lee, H.; Zhang, J.; Jiang, H.; Fang, N. X. *Phys. Rev. Lett.* **2012**, *108*, 214304.
- (12) Crescitelli, A.; Ricciardi, A.; Consales, M.; Esposito, E.; Granata, C.; Galdi, V.; Cutolo, A.; Cusano, A. *Adv. Funct. Mater.* **2012**, *22*, 4389.
- (13) Jeon, H. C.; Heo, C. J.; Lee, S. Y.; Yang, S. M. *Adv. Funct. Mater.* **2012**, *22*, 4268.
- (14) Yang, S. K.; Cai, W. P.; Kong, L. C.; Lei, Y. *Adv. Funct. Mater.* **2010**, *20*, 2527.
- (15) Wang, Y.; Becker, M.; Wang, L.; Liu, J. Q.; Scholz, R.; Peng, J.; Gosele, U.; Christiansen, S.; Kim, D. H.; Steinhart, M. *Nano Lett.* **2009**, *9*, 2384.
- (16) Chen, Z. G.; Zou, J.; Liu, G.; Yao, X. D.; Li, F.; Yuan, X. L.; Sekiguchi, T.; Lu, G. Q.; Cheng, H. M. *Adv. Funct. Mater.* **2008**, *18*, 3063.



- (17) Singh, G.; Griesser, H. J.; Bremmell, K.; Kingshott, P. *Adv. Funct. Mater.* **2011**, *21*, 540.
- (18) Chen, W. Q.; Villa-Diaz, L. G.; Sun, Y. B.; Weng, S. N.; Kim, J. K.; Lam, R. H. W.; Han, L.; Fan, R.; Krebsbach, P. H.; Fu, J. P. *ACS Nano* **2012**, *6*, 4094.
- (19) Yamaguchi, S.; Yamahira, S.; Kikuchi, K.; Sumaru, K.; Kanamori, T.; Nagamune, T. *Angew. Chem., Int. Ed.* **2012**, *51*, 128.
- (20) Singh, G.; Gohri, V.; Pillai, S.; Arpanaei, A.; Foss, M.; Kingshott, P. *ACS Nano* **2011**, *5*, 3542.
- (21) Ogaki, R.; Lyckegaard, F.; Kingshott, P. *ChemPhysChem* **2010**, *11*, 3609.
- (22) Pallandre, A.; Glinel, K.; Jonas, A. M.; Nysten, B. *Nano Lett.* **2004**, *4*, 365.
- (23) Urban, J. J.; Talapin, D. V.; Shevchenko, E. V.; Kagan, C. R.; Murray, C. B. *Nat. Mater.* **2007**, *6*, 115.
- (24) Ristenpart, W. D.; Aksay, I. A.; Saville, D. A. *Phys. Rev. Lett.* **2003**, *90*, 128303.
- (25) Singh, G.; Pillai, S.; Arpanaei, A.; Kingshott, P. *Adv. Funct. Mater.* **2011**, *21*, 2556.
- (26) Duan, H. G.; Hu, H. L.; Kumar, K.; Shen, Z. X.; Yang, J. K. W. *ACS Nano* **2011**, *5*, 7593.
- (27) Park, K.-C.; Choi, H. J.; Chang, C.-H.; Cohen, R. E.; McKinley, G. H. *ACS Nano* **2012**, *6*, 3789.
- (28) Lian, J.; Wang, L. M.; Sun, X. C.; Yu, Q. K.; Ewing, R. C. *Nano Lett.* **2006**, *6*, 1047.
- (29) Hulteen, J. C.; Van Duyne, R. P. *J. Vac. Sci. Technol., A* **1995**, *13*, 1553.
- (30) Kosiorek, A.; Kandulski, W.; Glaczynska, H.; Giersig, M. *Small* **2005**, *1*, 439.
- (31) Li, Y.; Koshizaki, N.; Cai, W. P. *Coord. Chem. Rev.* **2011**, *255*, 357.
- (32) Zhang, J.; Yang, B. *Adv. Funct. Mater.* **2010**, *20*, 3411.
- (33) Vogel, N.; Fischer, J.; Mohammadi, R.; Retsch, M.; Butt, H.; Land-Fester, K.; Weiss, C. K.; Kreiter, M. *Nano Lett.* **2011**, *11*, 446.
- (34) Gwinner, M. C.; Koroknay, E.; Fu, L. W.; Patoka, P.; Kandulski, W.; Giersig, M.; Giessen, H. *Small* **2009**, *5*, 400.
- (35) Retsch, M.; Tamm, M.; Bocchio, N.; Horn, N.; Forch, R.; Jonas, U.; Kreiter, M. *Small* **2009**, *5*, 2105.
- (36) Li, Y.; Fang, X. S.; Koshizaki, N.; Sasaki, T.; Li, L.; Gao, S. Y.; Shimizu, Y.; Bando, Y.; Golberg, D. *Adv. Funct. Mater.* **2009**, *19*, 2467.
- (37) Yang, S. K.; Lapsley, M. I.; Cao, B.; Zhao, C.; Zhao, Y.; Hao, Q.; Kiraly, B.; Scott, J.; Li, W.; Wang, L.; Lei, Y.; Huang, T. J. *Adv. Funct. Mater.* **2013**, *23*, 720.
- (38) Li, C.; Hong, G. S.; Qi, L. M. *Chem. Mater.* **2010**, *22*, 476.
- (39) Yang, S. K.; Cai, W. P.; Yang, J. L.; Zeng, H. B. *Langmuir* **2009**, *25*, 8287.
- (40) Yang, S. K.; Kiraly, B.; Wang, W. Y.; Shang, S.; Cao, B.; Zeng, H.; Zhao, Y.; Li, W.; Liu, Z.-K.; Cai, W.; Huang, T. J. *Adv. Mater.* **2012**, *24*, 5598.
- (41) Linic, S.; Christopher, P.; Ingram, D. B. *Nat. Mater.* **2011**, *10*, 911.
- (42) Warren, S. C.; Thimsen, E. *Energy Environ. Sci.* **2012**, *5*, 5133.
- (43) Herminghaus, S.; Jacobs, K.; Mecke, K.; Bischof, J.; Fery, A.; Ibn-Elhaj, M.; Schlagowski, S. *Science* **1998**, *282*, 916.
- (44) Thiele, U.; Mertig, M.; Pompe, W. *Phys. Rev. Lett.* **1998**, *80*, 2869.
- (45) Bischof, J.; Scherer, D.; Herminghaus, S.; Leiderer, P. *Phys. Rev. Lett.* **1996**, *77*, 1536.
- (46) Lal, S.; Grady, N. K.; Kundu, J.; Levin, C. S.; Lassiter, J. B.; Halas, N. J. *Chem. Soc. Rev.* **2008**, *37*, 898.
- (47) Li, Y.; Cai, W.; Cao, B.; Duan, G.; Li, C.; Sun, F.; Zeng, H. J. *Mater. Chem.* **2006**, *16*, 609.
- (48) Ye, J.; Thompson, C. V. *Adv. Mater.* **2011**, *23*, 1567.
- (49) Jain, P. K.; Huang, W. Y.; El-Sayed, M. A. *Nano Lett.* **2007**, *7*, 2080.
- (50) Halas, N. J.; Lal, S.; Chang, W. S.; Link, S.; Nordlander, P. *Chem. Rev.* **2011**, *111*, 3913.
- (51) Ogaki, R.; Cole, M. A.; Sutherland, D. S.; Kingshott, P. *Adv. Mater.* **2011**, *23*, 1876.
- (52) Cobley, C. M.; Chen, J. Y.; Cho, E. C.; Wang, L. V.; Xia, Y. N. *Chem. Soc. Rev.* **2011**, *40*, 44.
- (53) Alvarez-Puebla, R. A.; Liz-Marzan, L. M. *Chem. Soc. Rev.* **2012**, *41*, 43.
- (54) Romanov, S. G.; Korovin, A. V.; Regensburger, A.; Peschel, U. *Adv. Mater.* **2011**, *23*, 2515.
- (55) Gao, H.; Yang, J.; Lin, J. Y.; Stuparu, A. D.; Lee, M. H.; Mrksich, M.; Odom, T. W. *Nano Lett.* **2010**, *10*, 2549.